

Clay interaction with liquid and supercritical CO₂: The relevance of electrical and capillary forces

D. Nicolas Espinoza*, J. Carlos Santamarina

School of Civil and Environmental Engineering, Georgia Institute of Technology, 790 Atlantic Drive, Atlanta, GA 30332-0355, USA

ARTICLE INFO

Article history:

Received 6 August 2011
Received in revised form 18 May 2012
Accepted 26 June 2012
Available online 25 July 2012

Keywords:

Carbon geological storage
Cap rock
Phyllosilicates
Mineral fluid interaction
Swelling pressure
Desiccation crack
Sealing capacity

ABSTRACT

Caprocks with significant clay content are candidate seal layers for CO₂ geological storage. Changes in electrical and capillary forces are expected when CO₂ invades the water saturated pore space. Sedimentation experiments conducted to explore the response of kaolinite and montmorillonite to deionized water, brine, heptane, liquid CO₂ and supercritical CO₂ show that both montmorillonite and kaolinite aggregate when submerged in CO₂ and the final porosity in CO₂ is smaller than in brine. Differences in dielectric properties between CO₂ and water, and ensuing implications on van der Waals attraction and double layer repulsion explain the observed phenomena. On the other hand, capillary effects induced by the water–CO₂ interface are corroborated by clay–water paste desiccation experiments conducted using supercritical CO₂: water dissolution into the surrounding CO₂ causes suction and capillary contraction, the invasion of the CO₂–water interface into the sediment, and the formation of desiccation cracks. Volume contraction and crack initiation are consistent with the sediment response within an effective stress framework. Altered electrical forces and emergent capillary forces lead to coupled chemo-hydro-mechanical phenomena in seal layers that could facilitate CO₂ breakthrough and advection through high porosity caprocks; related phenomena are identified in the reservoir rock. Additional studies are needed to further assess coupled phenomena when the interparticle distance is a few monolayers of water.

© 2012 Elsevier Ltd. All rights reserved.

1. Introduction

Carbon capture and geological storage have been proposed to reduce greenhouse gas emissions into the atmosphere. CO₂ would be captured at concentrated point sources (typically power plants), and then compressed and injected into nearby geological formations (IPCC, 2005). Most carbon storage target sites, such as deep saline formations, consist of high permeability and porosity repositories to store pressurized and buoyant CO₂, overlaid by a low permeability sealing caprock (see Fig. 1 – Dooley et al., 2006; Gale, 2004). Two important macro-scale characteristics of good seal layers are continuity and ductility (Downey, 1984). Faults, fractures, and existing wellbores are major discontinuities and may result in preferential paths for CO₂ leakage. On the other hand, ductility allows caprock deformation without fracturing.

Shales and evaporites commonly serve as caprocks for natural hydrocarbon accumulations; similarly these rocks are considered as potential seal layers for CO₂ storage. Shales are made of clay minerals, fine-grained quartz, feldspar and carbonates, with particle size typically less than 60 μm (Gueguen and Palciauskas,

1994). Table 1 shows a compilation of petrographical properties of shale caprocks at selected carbon storage sites; clay minerals are a major component of these rocks. Evaporite seal layers serve as CO₂ caprocks at Weyburn, the K12-B project, and the Salt Creek CO₂ injection site (Benison and Goldstein, 2000; Chiaramonte et al., 2008; Li et al., 2005; Vandeweyer et al., 2011).

Clay minerals control the mechanical and transport properties of shales. Clay minerals are phyllosilicates that crystallize in small-size platy grains, typically <10 μm (Mitchell and Soga, 2005; Sposito, 1989). Burial and diagenesis at high temperature and pressure compact shales and reduce the pore size (Nygard et al., 2004). The mean pore size of shales ranges from 5 nm to 100 nm, porosity from ~1% to 12%, and permeability from 10⁻²² m² to 10⁻¹⁹ m² (Armitage et al., 2010; Katsube and Williamson, 1994; Watson et al., 2005).

The sealing efficiency of intact shale caprocks is dominated by high specific surface clays. Fine grained clays can resist high capillary entry pressures, but are more susceptible to changes in electrical forces. Capillary forces and changes in electrical interactions will inherently arise as CO₂ invades the caprock because of the CO₂–water interfacial tension, water acidification, and the nonpolarity of CO₂. Eventually, capillary and electrical phenomena upscale, causing mechanical couplings which will affect porosity, clay fabric, hydraulic conductivity, compressibility, and shear

* Corresponding author.

E-mail address: nicolas.espinoza@gatech.edu (D.N. Espinoza).

Symbols

β	particle slenderness []
δ	reduction in interparticle distance []
ε	strain []
ε_0	permittivity constant: 8.854×10^{-12} C/(J m)
ζ	Debye-Hückel length [m]
η	refractive index []
θ	contact angle []
κ'	relative permittivity []
ν_e	electrical relaxation frequency [Hz]
ρ	mass density [kg/m ³]
σ'	effective stress [Pa]
A_h	Hamaker constant [J]
C_c	Sediment compressibility coefficient []
F	Faraday constant: 96485.3 C/mol
F_{type}	force type [N]
R	gas universal constant: 8.314 J/(mol K)
S_s	specific surface [kg/m ²]
T	temperature [K]
V	volume [m ³]
c_0	ionic concentration [mol/L]
d	particle size [m]
e	void ratio []
h	Planck's constant: 6.626×10^{-34} J s
l	particle length [m]
m	mass [kg]
n	porosity []
s	interparticle distance [m]
t	platelet thickness [m]

strength (similarly to NAPL and clays; Jo et al., 2001; Kaya and Fang, 2005; Montoro and Francisca, 2010; Santamarina et al., 2001b). Yet, the interaction between clay minerals and CO₂ is poorly understood. A limited number of studies address the behavior of clay minerals surrounded by CO₂ including gas sorption experiments (Busch et al., 2008), X-ray diffraction experiments (Giesting et al., 2012; Ilton et al., 2012; Schaefer et al., 2012), molecular simulations (Botan et al., 2010), solute extraction from clay using supercritical fluids (Fahmy et al., 1993), and polymer manufacturing investigations (Serhatkulu et al., 2006; Urbanczyk et al., 2010).

In this study, we explore the interaction between liquid and supercritical CO₂ with clay minerals to gain insight into complex phenomena relevant to CO₂ storage conditions. The study starts with an assessment of particle-level forces in clay–water–CO₂ systems; then experimental evidence gathered in simple and well constrained experiments is presented. Finally, the study concludes with an analysis of anticipated geomechanical and hydrological implications for CO₂ storage sites that involve clayey caprocks.

2. Preliminary analysis of clay–water–CO₂ systems

Particle-level forces can be grouped into (Santamarina, 2001; van Oort, 2003): (1) mechanical, including skeletal forces due to effective stress, seepage-drag, capillarity, and passive cementation forces and (2) electrical, including van der Waals attraction, Born repulsion, and electrical forces due to double layer formation, surface hydration and osmotic effects. Because of their physico-chemical nature, electrical forces depend on the pore fluid chemistry. The following analysis of electrical and mechanical particle-level forces is conducted to assess their relevance in the context of CO₂ geological storage.

2.1. Electrical forces

The surface charge of clay particles is pH dependent: the abundance of H⁺ at low pH promotes protonation leading to positively charged surfaces (Lyklema, 1995; Santamarina et al., 2001a; Stumm, 1992). Note: Implications of acidification, such as in CO₂ storage, on surface charge and clay fabric are discussed in Palomino and Santamarina (2005).

Hydrated ions interact with the charged clay surfaces and form the diffuse counter-ion cloud; the ensuing interparticle repulsion increases with the pore fluid relative permittivity κ' and it is inversely proportional to the pore fluid ionic strength c_0 . On the other hand, van der Waals interactions give rise to attraction forces between clay minerals; this force is proportional to the Hamaker constant which is a function of the permittivity of the fluid and minerals involved. Additional molecular-scale processes must be recognized in this analysis: (1) when a water-saturated clay dries, counter ions bind to the particle surface and excess salts precipitate; (2) the hydration/dehydration state of montmorillonite differs according to relative humidity and interlayer cation (Ferrage et al., 2005); (3) typical computations of double layer repulsion and van der Waals attraction forces apply to systems where the interparticle distance is much larger than the size of molecules; and (4) short-range Born repulsion and periodically varying hydration forces must be considered at interparticle distances smaller than ~ 2 nm (Israelachvili, 1991; van Oort, 2003).

Changes in pore fluid chemistry (ionic concentration c_0 , pH, relative permittivity κ') and their impact on electrical interactions have complex consequences on the sediment volume change and its hydraulic and mechanical properties. The role of these surface phenomena is proportional to the specific surface of the clay sediment.

2.2. Capillary forces: interfacial tension and contact angle

The water–CO₂ interfacial tension is pressure-temperature dependent. It decreases from $T_s \sim 72$ to 25 mN/m as the pressure increases from 0.1 MPa to 6.4 MPa at ~ 298 K. Eventually T_s reaches a plateau at $T_s = 25 \pm 5$ mN/m in the supercritical CO₂ state; high salinity increases the brine–CO₂ interfacial tension by ~ 10 mN/m above water–CO₂ values (Chalbaud et al., 2009; Espinoza and Santamarina, 2010). The contact angle formed by the water–CO₂ interface on mineral surfaces varies with fluid pressure in response to changes in water–CO₂ interfacial tension: as the fluid pressure increases to reservoir conditions, the contact angle increases on oil-wet amorphous silica ($\theta \sim 85$ – 95°), coal ($\theta \sim 50$ – 120°) and mica ($\theta \sim 40$ – 60°), and it decreases slightly in water-wet amorphous silica and calcite surfaces ($\theta \sim 40^\circ$) (Chalbaud et al., 2009; Chi et al., 1988; Chiquet et al., 2007; Dickson et al., 2006; Espinoza and Santamarina, 2010). The measurement of contact angle on fine-grained sediments is not straight forward due to heterogeneities, particle orientation and the development of suction. The film flotation and spontaneous/forced imbibition techniques can help characterize wettability in fine-grained sediments (Borysenko et al., 2009). Together, interfacial tension T_s and contact angle θ determine the magnitude of capillary phenomena ($T_s \cos \theta$). The interaction between capillary phenomena and mechanical stress is critical to evaluate hydro-mechanical couplings (Alonso et al., 1990).

2.3. Particle forces and strains

Let's estimate the effect of water displacement by CO₂ on interparticle interactions (details can be found in Santamarina, 2001; Santamarina et al., 2001a). The capillary force computed for a water meniscus between two platy particles thickness t , length

Table 1
Petrographical properties of caprocks at selected carbon storage sites.

Site	Dominant clay minerals [weight %]	Other minerals	Approximate overburden depth (m)	Porosity (%)
Frio, USA (Hovorka, 2009; Lynch, 1997)	Illite-smectite ~45% Illite ~10% Kaolinite 13% Chlorite ~3%	Calcite	1450	8–10
Sleipner, Norway (Bøe and Zweigel, 2001; Chadwick et al., 2004; Pilliteri et al., 2003)	Mica-Illite ~25% Kaolinite 14–18% Smectite 3–9% Chlorite 1–4%	Calcite 1–3% Siderite 2%	750	35
Krechba, Algeria (Armitage et al., 2010; Mathieson et al., 2010)	Muscovite-illite ~25–50% Chlorite ~20–4% Kaolinite ~8–4%	Siderite ~15–0%	1850	1.8–11.3
Otway, Australia (Watson et al., 2005)	Kaolinite 44–17% Illite 6–1% Smectite 3–1%	Siderite 35–2%	1980	2.5–7.5
SACROC, USA (Carey et al., 2007; Han et al., 2010)	Illite-smectite 62%	Calcite 2.5% Dolomite 2% Halite 0.1%	2000	1.3
Rousse, France (Tonnet et al., 2011)	Illite 2.2–14.5% Kaolinite 0.3–4.1% Chlorite 0.1–2%	Calcite 30–65% Dolomite 3–63% Siderite 0.1–6.2%	4000	0.5–3
Carnarvon, Australia (Dewhurst et al., 2002)	Illite-smectite 30–25% Illite 15–20% Kaolinite ~15% Chlorite ~5%	Siderite 1–4%	1100	21
Ketzin, Germany (Förster et al., 2007)	Illite 42–74% Chlorite 1–3%	Dolomite 4–35% Halite (small fraction)	600	10

l , slenderness $\beta = l/t$, mineral mass density ρ_m and specific surface $S_s = 2(1 + 2/\beta)/(t\rho_m)$ in a shale with porosity n is (assumed contact angle $\theta \sim 0^\circ$),

$$F_{\text{cap}} = S_s \rho_m T_s \frac{1-n}{n} l^2 = S_s \rho_m T_s \frac{1-n}{n} \beta^2 \left[\frac{2(1+2/\beta)}{S_s \rho_m} \right]^2 \quad (1)$$

On the other hand, the average force carried by a particle within a granular skeleton subjected to an effective stress σ' is

$$F_{\text{sk}} = \sigma' \left(\frac{\beta^2}{1-n} \right)^{2/3} \left[\frac{2(1+2/\beta)}{S_s \rho_m} \right]^2 \quad (2)$$

The ratio between these forces is

$$\frac{F_{\text{cap}}}{F_{\text{sk}}} = \rho_m T_s \frac{S_s (1-n)^{5/3}}{\sigma'} \frac{\beta^{2/3}}{(1+2/\beta)} \quad (3)$$

The colinearity of electrical forces and skeletal forces hinders a force-based comparison. Instead, let's estimate the impact of a reduction δ in interparticle separation s as a result of a decrease in electrical repulsion forces and an increase in van der Waals attraction. The corresponding strain ε is

$$\varepsilon = \frac{\rho_m}{2} \delta S_s (1-n) \quad (4)$$

Fig. 2 shows a plot of the force ratio $F_{\text{cap}}/F_{\text{sk}}$ and of the shrinkage strain versus specific surface in the context of carbon geological storage. We identify two zones:

- **Reservoir domain:** Grains are large (particle size $d > 10^{-6}$ m) and rotund, and their specific surface is low. Contact forces F_{sk} due to effective stress prevail (note: capillarity and mixed fluid

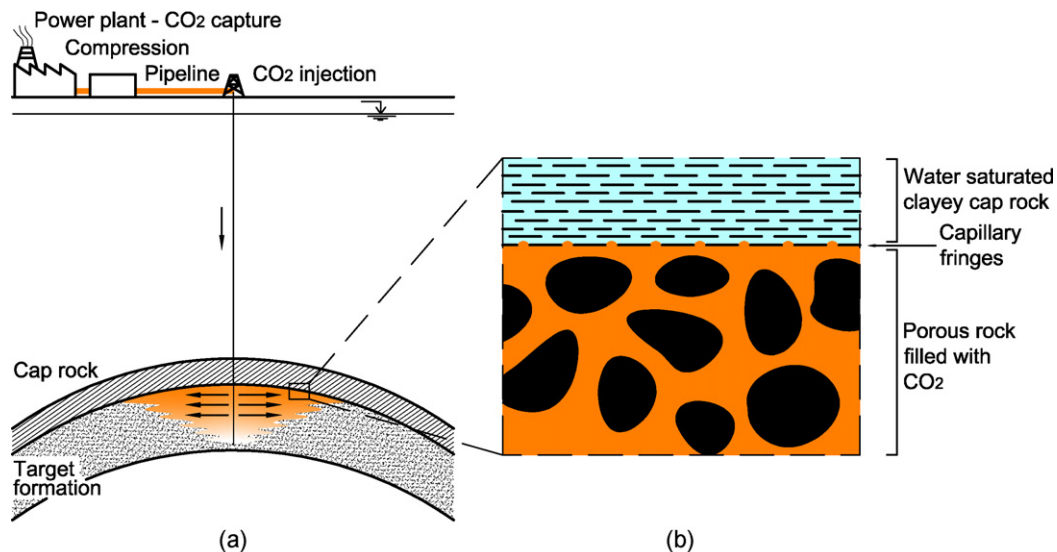


Fig. 1. Carbon capture and geological storage. (a) A power plant equipped with carbon capture technology delivers CO₂ to the storage site where CO₂ is injected into a porous formation overlaid by a caprock. (b) Close-up of shale-sandstone interface where pressurized buoyant CO₂ is retained by capillary fringes.

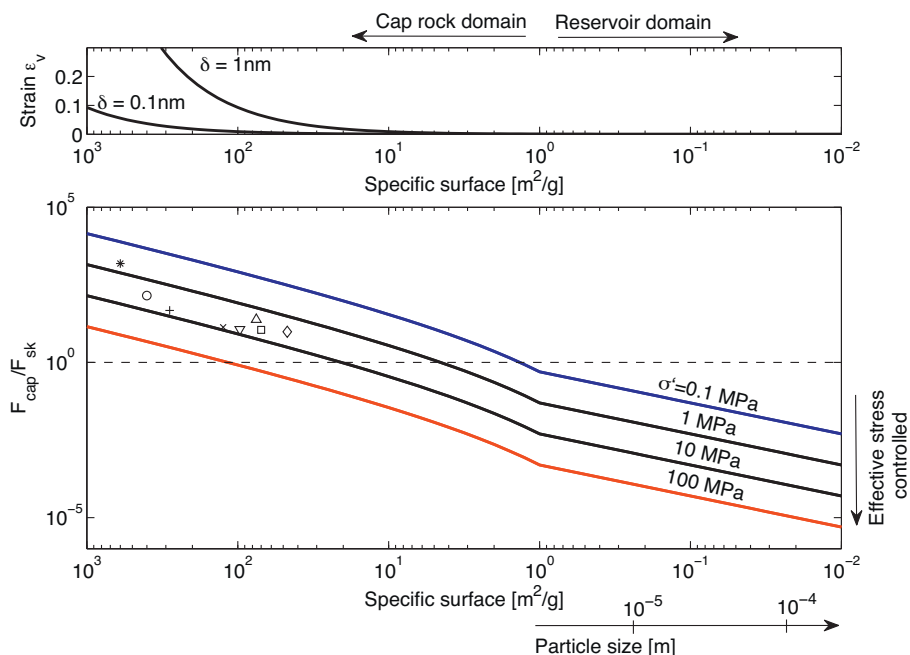


Fig. 2. Relevance of physico-chemical phenomena in geological formations used for CO₂ storage – Particle scale analysis. Ratio of capillary to skeletal forces (Eq. (3)) and strain due to reduction in interparticle distance with changes in electrical forces (Eq. (4) – initial porosity 0.3) versus specific surface. The symbols represent conditions of caprocks at Frio (○), Sleipner (×), Krechba (□) and Otway (◇), SACROC (*), Rouse (△), Carnarvon (+), Ketzin (▽). In each case, the specific surface is estimated from reported clay composition, and the effective stress is estimated from the overburden depth (details and references in Table 1). The particle slenderness is assumed to be $\beta = 1$ for $S_s < 1 \text{ m}^2/\text{g}$ and $\beta = (1 + (\log(S_s/(1 \text{ m}^2/\text{g})))^{2.5})$ for $S_s > 1 \text{ m}^2/\text{g}$.

conditions do affect fluid flow in this domain). Strains due to changes in electrical forces are negligible.

- **Caprock domain:** Capillary forces and physico-chemical electrical interactions gain relevance when small particles are involved, as in caprocks (particle size $d < 10^{-6} \text{ m}$).

Specific surface $S_s = 2/(d\rho_m)$ [m^2/g] is an adequate physical quantity for characterizing platy fine grained sediments and it is intimately linked to the clay composition in the caprock (e.g., $S_s \sim 400\text{--}700 \text{ m}^2/\text{g}$ for montmorillonite, $50\text{--}100 \text{ m}^2/\text{g}$ for illite and $5\text{--}10 \text{ m}^2/\text{g}$ for kaolinite, Mitchell and Soga, 2005; Santamarina et al., 2002; Van Olphen, 1977). We use these S_s values and clay composition from Table 1 to estimate caprock specific surface at CO₂ storage sites. Computed $F_{\text{cap}}/F_{\text{sk}}$, ε , and specific surfaces values for selected caprocks are superimposed on the Fig. 2.

2.4. Observations

Results show that physico-chemical effects must be taken into consideration when high specific surface clayey rocks are selected as caprocks for CO₂ storage, including sites that are currently being considered.

It is important to highlight that the previous analyses consider forces and concepts such as interfacial tension that apply to large interparticle distances. Further analyses are needed to explore these coupled phenomena when the interparticle distance is equivalent to a few monolayers of water, as in mormorillonitic shales.

3. Study of electrical forces – sedimentation tests

Observations in the previous section showed the importance of physico-chemical effects in clayey caprocks. The purpose of this section is to further explore differences in clay behavior in non-polar CO₂ versus polar water. Sedimentation tests are used to magnify the effects of electrical interactions between fine grained clay particles.

3.1. Device, materials, and experimental procedure

Sedimentation tests were conducted in a polycarbonate tube (effective height 95 mm, ID=6.35 mm and OD=19.0 mm) held between aluminum caps, and sealed with buna-N o-rings (Fig. 3a). Pressure transducers and thermocouples track pressure–temperature conditions. Time-lapse photography is used to monitor and record all experiments.

Two clays were selected for this study: kaolinite SA1 (1:1 clay provided by Wilkinson; details in Palomino, 2003) and calcium montmorillonite (2:1 clay, montmorillonite-rich bentonite Panther Creek 150 from the American Colloid Company; additional characterization in Hundal et al., 2001). Sedimentation tests were conducted with different polar and non-polar fluids including deionized/deaerated water, brine consisting of 2 M NaCl aqueous solution, heptane (Fisher Scientific), and research grade CO₂ (Air-gas). Tables 2 and 3 summarize the physical properties of clays and fluids used in these experiments. Depending on the fluid, experiments were performed at atmospheric pressure or at 7–12 MPa (see Table 3).

The experimental procedure consists of five sequential steps: (1) fill the tube with clay ($\sim 0.06 \text{ g}$, i.e., the solids volume fraction is less

Table 2
Clays used in these experiments – physical properties.

Physical property	Kaolinite	Montmorillonite
Mineralogy	1:1	2:1
Specific surface* S_s [m^2/g]	50–55	610–670
Particle thickness** t [m]	15×10^{-9}	1×10^{-9}
Specific gravity G_s []	2.6	2.7
Liquid limit*** LL [%]	45	250
Static relative permittivity κ' (a)	5.1	5.5
Refractive index in visible range η (b)	1.56	1.5

Note: (*) Measured with methylene blue spot technique (Santamarina et al., 2002); (**) estimated from $t \sim 2/(S_s \rho_w G_s)$; (***) fall cone test. Refs.: (a) Robinson (2004); (b) Leach et al. (2005), Weidler and Friedrich (2007).

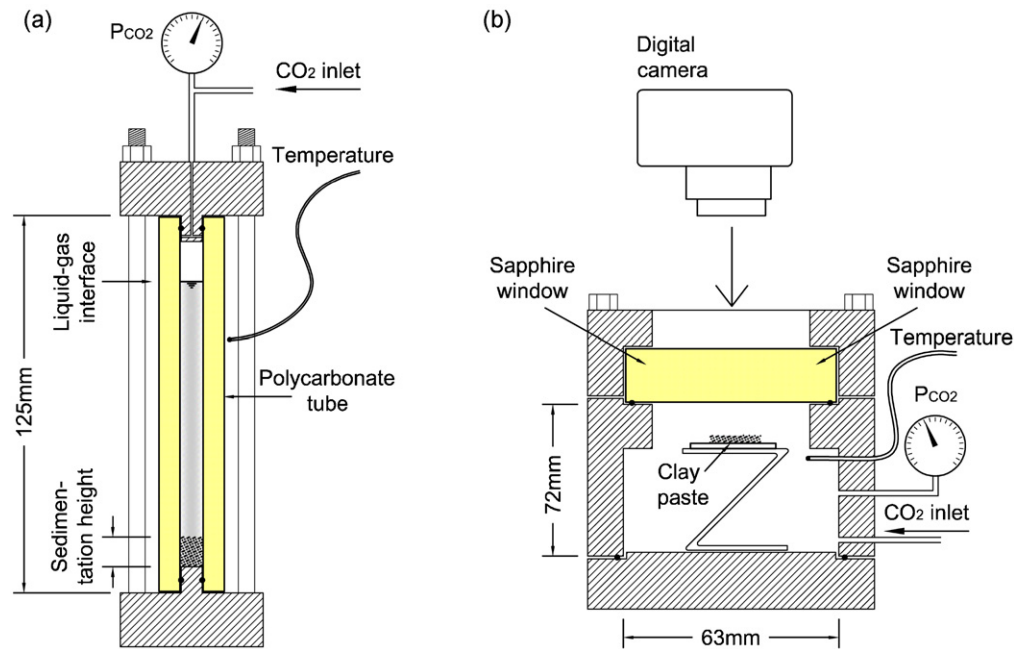


Fig. 3. Experimental devices. (a) Sedimentation tube: the transparent polycarbonate tube (ID = 6.35 mm) is held between two aluminum caps with buna-N o-rings; external transducers measure pressure and temperature. (b) High pressure chamber equipped with a see-through sapphire window: the clay paste is placed on a glass slide; the large chamber volume compared to the paste volume allows a significant water mass to dissolve into the scCO₂ that fills the chamber.

Table 3
Fluids used for sedimentation experiments – physical properties.

Physical property (test condition)	Water (0.1 MPa, 298 K)	Brine, 2 M NaCl (0.1 MPa, 298 K)	Heptane (0.1 MPa, 298 K)	Supercritical CO ₂ (12 MPa, 313 K)	Liquid CO ₂ (7 MPa, 298 K)
Density ρ [kg/m ³]	997	1072 (a)	680 (b)(g)	719 (c)	745 (c)
Viscosity μ [Pa·s]	0.90×10^{-3} (a)	1.08×10^{-3} (a)	0.386×10^{-3} (b)	0.059×10^{-3} (d)	0.0620×10^{-3} (d)
Polarity	Polar	Polar	Non-polar	Non-polar	Non-polar
Static permittivity κ' (at 1 GHz)	78.5 (e)	56 (f)	1.92 (g)	1.43 (h)	1.46 (m)
Refractive index η (visible range)	1.333 (e)	~1.36 (n)	1.385	1.169 (h)	1.175 (m)
Hamaker constant A_h^\dagger [10^{-20} J]	1.57 k–w–k	1.24 k–b–k	0.84 k–h–k	4.2 k–scCO ₂ –k	4.0 k–ICO ₂ –k
	0.98 m–w–m	0.73 m–b–m	0.42 m–h–m	3.1 m–scCO ₂ –m	3.0 m–ICO ₂ –m
				1.1 w–scCO ₂ –w	1.0 w–ICO ₂ –w
Solubility of water [mol H ₂ O/mol fluid]	NA	NA	$0.5\text{--}0.6 \times 10^{-3}$ (k)	4.5×10^{-3} (j)	2.9×10^{-3} (j)
Interfacial tension with water T_s [Nm]	NA	NA	0.051 (o)	0.028 (p)	0.030 (q)

Note: (\dagger) Calculated using Lifschitz theory, Eq. (9) (m: montmorillonite, k: kaolinite, w: water, b: brine, h: heptane).

Refs.: (a) Zhang and Han (1996); (b) Aucejo et al. (1995); (c) Span and Wagner (1996); (d) Fenghour et al. (1998); (e) Israelachvili (1991); (f) Buchner et al. (1999), Santamarina et al. (2001b); (g) Friiso and Tjomsland (1997); (h) Obriot et al. (1993), Sun et al. (2003); (j) Spycher et al. (2003); (k) Polak and Lu (1973); Susilo et al. (2005); (m) Lewis et al. (2001), May et al. (2005); (n) Maykut and Light (1995); (o) Zeppieri et al. (2001); (p) Kvamme et al. (2007); (q) Espinoza and Santamarina (2010).

than 0.01), (2) subject the air-dry clay to vacuum at 340 K for 24 h to remove part of the adsorbed water, (3) fill the tube with the selected fluid (~2.5 ml, note that non-removed adsorbed water might mix or dissolve in the selected fluid), (4) shake the cell to thoroughly

mix the fluid and clay into a colloidal suspension, and (5) place the tubes vertically, allowing the clay to settle at the bottom of the tubes. This procedure is repeated several times for each clay–fluid combination (2 clays and 5 fluids, see Table 4). We measure the

Table 4
Summary of sedimentation results.

Fluid	Water	Brine	Heptane	Liquid CO ₂	Supercritical CO ₂
Kaolinite $M_{\text{clay}} = 0.060$ g					
Number of experiments	12	6	4	5	2
Final height h [mm]	6.3 (5.3–7.9)	6.7 (6.2–7.5)	8.9 (8.0–9.5)	7.1 (6.7–7.5)	3.3* (3.0–3.6)
Floc size [μm]	4–43	50–94	370–610	280–550	88–220
Montmorillonite $M_{\text{clay}} = 0.056$ g					
Number of experiments	5	3	3	4	4
Final height h [mm]	NA (cloudy)	6.0 (5.5–6.2)	2.0 (1.9–2.1)	2.7 (2.4–2.9)	2.4 (2.0–2.7)
Floc size [μm]	<0.7	48–127	41–165	47–94	47–142

Note: (*) result biased by clay attachment to the tube walls.

settling rate, sedimentation height, and observe particle agglomeration and flocculation following the test procedure outlined in Palomino (2003).

3.2. Results

Sedimentation patterns, such as final sediment height, aggregate size and sedimentation mode, change noticeably with different pore fluids; these characteristics are summarized in Table 4. For example, montmorillonite remains in suspension for days in distilled water, but it aggregates and settles in a matter of seconds in supercritical CO₂ (Fig. 4). Details follow (Table 4).

Flocculation/aggregation. Both clays flocculate in brine. The diameter of kaolinite and bentonite aggregations in brine is inferred from Stokes' law (laminar regime expected at low sedimentation velocity v_s), $d_{eq} = [18 v_s \mu g^{-1} (\rho_{floc} - \rho_{fluid})^{-1}]^{1/2} = 50\text{--}140 \mu\text{m}$, and it is 2 orders of magnitude larger than the actual particle size. In these estimations, the assumed aggregate density is $\rho_{floc} = \rho_f n + \rho_m (1 - n)$, where ρ_f and ρ_m are the fluid and mineral mass densities and n is the final sedimentation porosity.

Both kaolinite and montmorillonite show extensive particle aggregation when suspended in low permittivity fluids (heptane, liquid CO₂ and supercritical CO₂ – see Table 4 and Figs. 4 and 5). Due to fast sedimentation, aggregate sizes are determined from high-resolution images analysis and range from ~90 to 600 μm for kaolinite and up to 160 μm for montmorillonite.

Additional experiments performed with air-dry montmorillonite and CO₂ (not shown in Figures and Tables) show massive agglomeration. Evidently, repulsive CO₂–water interaction promotes the agglomeration of clay particles with excess adsorbed water on their surfaces when suspended in liquid or supercritical CO₂. Similar clay behavior changes with adsorbed water have been reported in the literature (Fahmy et al., 1993; Ilton et al., 2012).

Solubility analyses anticipate that as much as ~5 mg of water can be dissolved in the 3 cm³ of bulk CO₂ inside the sedimentation cell at current experimental conditions (water solubility in CO₂ data from Spycher et al., 2003). This mass is equivalent to the mass of one monolayer of water adsorbed on the montmorillonite specimen and more than 10 times the mass of a monolayer of water adsorbed on the kaolinite specimen. Yet, adsorbed water is not necessarily removed from the clay surface; X-ray diffraction experiments show that anhydrous CO₂ ($P=9\text{--}18 \text{ MPa}$ and $T=50\text{--}100 \text{ }^\circ\text{C}$) can extract water from 2W state montmorillonite producing a shrinkage of the basal spacing $\Delta d_{001} \sim 12.52\text{--}14.48 = -2 \text{ \AA}$, but cannot extract adsorbed water from 1W state montmorillonite (Giesting et al., 2012; Schaefer et al., 2012).

Sediment final porosity. The final sediment height h is used to compute the sediment final porosity from the total volume V_T and the volume of solids V_S (values in Table 4):

$$n = \frac{V_T - V_S}{V_T} = 1 - \frac{M_{\text{clay}}/\rho_m}{1/4 \cdot \pi D^2 h} \quad (5)$$

where M_{clay} is the clay mass, ρ_m is the mass density of the clay mineral, and D is the tube inside diameter. Results are plotted in Fig. 5. In general, aggregations are largest and the sediment porosity is minimal in heptane and CO₂. Aggregate size increases and porosity decreases with ionic concentration c_0 in aqueous suspensions. Pore fluid characteristics have a lesser effect on kaolinite than montmorillonite, and almost no effect on final porosity of kaolinite.

3.3. Analysis

Forces between suspended clay particles are governed by electrical interactions (mineralogy and pore fluid chemistry – Section 2). The double layer repulsion force can be estimated as

$$F_{\text{rep}} = 16\pi RT c_0 d^2 e^{-s/\zeta} \quad \text{for large } s > 2 \text{ nm} \quad (6)$$

The parameters in this equation are the diameter of disk-shaped particles d [m], the distance between discs s [m], the ideal gas constant $R=8.314 \text{ J}/(\text{mol K})$, the absolute temperature T [K], the bulk fluid ionic concentration c_0 [mol/L], and the Debye-Hückel length ζ for a $1/e$ decay of the Stern potential (Mitchell and Soga, 2005). This characteristic length ζ is

$$\zeta = \sqrt{\frac{1}{2} \frac{\epsilon_0 \kappa' RT}{c_0 z^2 F^2}} \quad (7)$$

where $\epsilon_0 = 8.854 \times 10^{-12} \text{ C}^2 \text{ J}^{-1} \text{ m}^{-1}$ is the real permittivity of free space, κ' is the relative permittivity of the solution, z is the valence of prevailing ions, and $F=96485.3 \text{ C/mol}$ is Faraday's constant.

On the other hand, the van der Waals electrostatic attraction force F_{att} between two disc-shaped clay particles diameter d suspended in a fluid with Hamaker constant A_h is (Israelachvili, 1991),

$$F_{\text{att}} = \frac{1}{24} A_h \frac{d^2}{s^3} \quad (8)$$

where s is the separation between the two particles. The Hamaker constant A_h depends on the dielectric properties of the mineral m and the fluid f , and can be estimated using Lifschitz' continuum theory in terms of the static relative permittivity κ' and the refractive index η in the visible range (valid for surface separations much greater than the molecule size – Israelachvili, 1991),

$$A_h = \frac{3}{4} k_B T \left(\frac{\kappa'_m - \kappa'_f}{\kappa'_m + \kappa'_f} \right)^2 + \frac{3h\nu_e}{16\sqrt{2}} \frac{(\eta_m^2 - \eta_f^2)^2}{(\eta_m^2 + \eta_f^2)^{3/2}} \quad (9)$$

where $k_B = 1.38 \times 10^{-23} \text{ J/K}$ is Boltzmann's constant, T [K] temperature, $h = 6.626 \times 10^{-34} \text{ J}\cdot\text{s}$ is Planck's constant, and ν_e is the electrical relaxation frequency, typically $\nu_e \sim 3 \times 10^{15} \text{ Hz}$. Properties and calculated values for the various clay–fluid systems under consideration are summarized in Table 3. The extreme scenario of mineral surfaces with no adsorbed water yields a Hamaker constant and attraction force ~3 times higher in mineral–CO₂–mineral than in mineral–water–mineral systems. The Hamaker constant for water–CO₂–water applies when the thickness of water layers is larger than the thickness of the CO₂ layer (Israelachvili, 1991).

The two electrical forces F_{rep} and F_{att} control the tendency for clay particles to agglomerate. Repulsion F_{rep} vanishes in non polar fluids (i.e., salts do not dissolve and ions do not hydrate). On the other hand, the Hamaker constant and F_{att} are higher when CO₂ fills the pore space rather than water. The evolution of these forces with permittivity explains the higher tendency to aggregate and the lower sedimentation volume in non-polar fluids, including CO₂ (note: ionic concentration c_0 and its effect on F_{rep} justify sedimentation differences in water and brine). We can conclude that volumetric contraction is expected as CO₂ displaces water from the clay pore space. This conclusion agrees with the observed dehydration of montmorillonite from 2W to 1W state when exposed to anhydrous CO₂ (Ilton et al., 2012; Schaefer et al., 2012).

The mean interparticle distance s can be estimated from the sediment porosity n or void ratio e and the platelet thickness t (See Table 2), assuming a parallel platelet fabric,

$$s = \frac{n}{1-n} t = e t \quad (10)$$

In the case of montmorillonite, the mean interparticle distance is $s \sim 8 \text{ nm}$ for the porosity of sediment in brine ($n \sim 0.88$) and $s = 2 \text{ nm}$

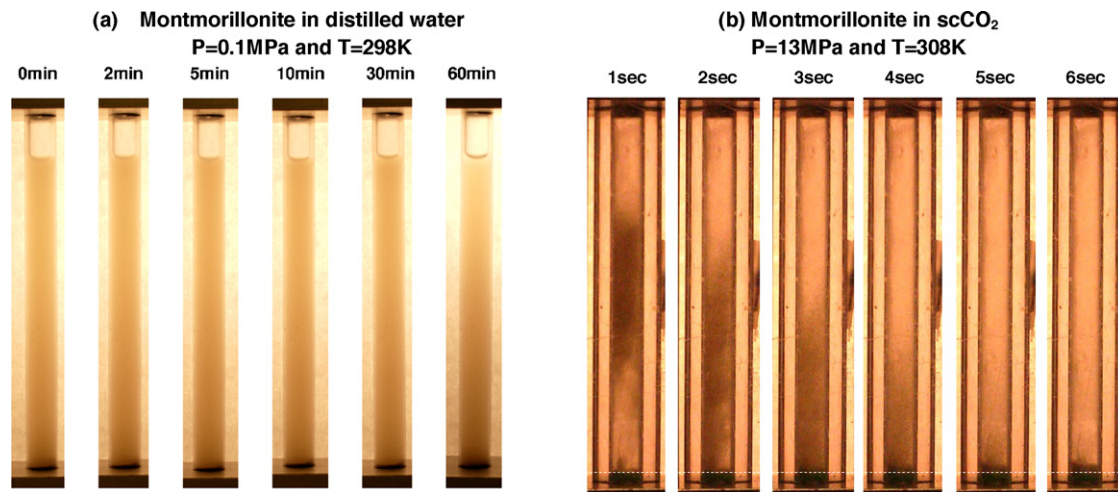


Fig. 4. Sedimentation study. Pictures of montmorillonite settling in (a) distilled water and (b) supercritical CO₂. Notice the pronounced difference in time scales. Montmorillonite particles remain dispersed and in suspension for days when the pore fluid is deionized water, however, they readily form 50–150 μm size flocs in scCO₂ and settle in few seconds. These pronounced differences in behavior reflect the role of governing electrical interparticle forces.

for the low final porosity measured in CO₂ ($n \sim 0.7$) assuming $t \sim 1$ nm. This interparticle separation is about two times the 1W state basal spacing $d_{001} \sim 12 \text{ \AA}$ measured in Ca–montmorillonite (Schaefer et al., 2012). In the case of kaolinite, the mean interparticle distance is $s \sim 135$ nm for the high porosity sediment in brine ($n \sim 0.9$) and $s = 35$ nm for the low porosity measured in CO₂ ($n \sim 0.7$) assuming $t \sim 15$ nm.

4. Study of capillary forces – desiccation tests

The particle level analysis presented earlier suggested pronounced capillary phenomena in clayey caprocks in the presence of water and CO₂ (Section 2). A special test is designed to corroborate

relevance of capillarity as the water–CO₂ interface invades the sediment pore space.

4.1. Device, materials, and experimental procedure

Three independent “desiccation experiments” were run by exposing clay–water to an anhydrous CO₂ atmosphere inside a stainless steel chamber at a temperature $T = 308$ – 313 K and pressure $P \sim 15$ MPa. We used the Panther Creek 150 calcium montmorillonite (see specifications in Section 3.1). The internal volume of the cylindrical chamber is 210 cm³ – Fig. 3b. A pressure transducer and a thermocouple are used to monitor pressure and temperature conditions inside the chamber and time-lapse photography is used to observe the evolution of the clay paste through a sapphire window.

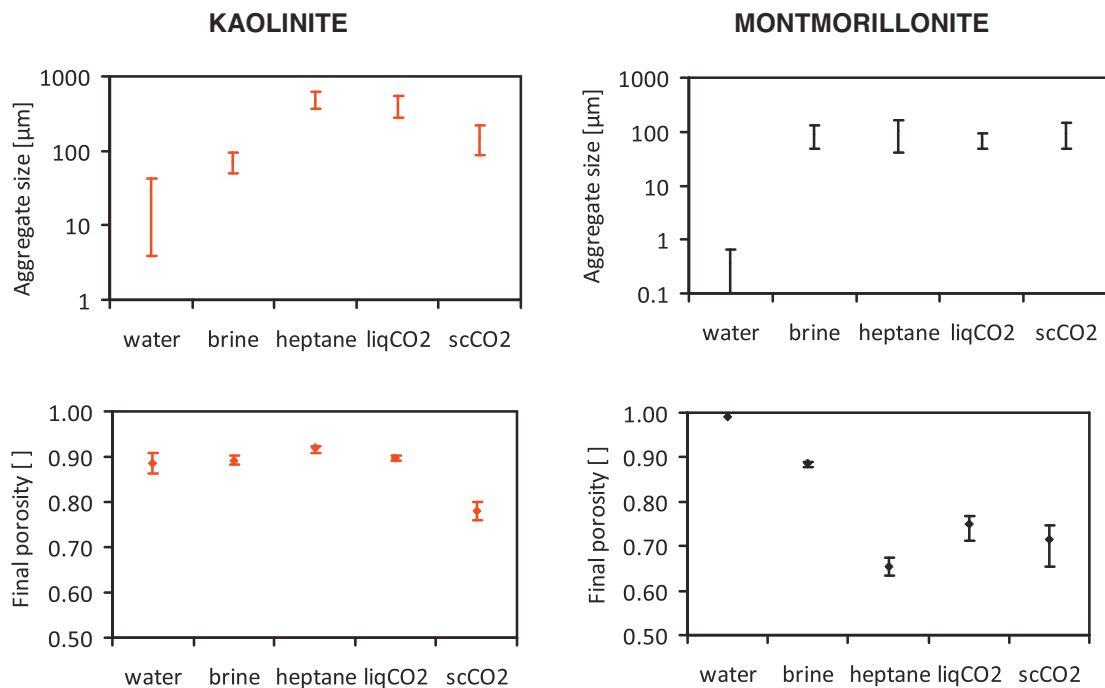


Fig. 5. Sedimentation test results: floc size and final porosity. The floc size in water and brine is computed using Stokes' law, and it is evaluated by direct visual measurement in heptane and CO₂. Notice the low sedimentation porosity of montmorillonite in supercritical CO₂. Significant particle aggregation is observed in both kaolinite and montmorillonite in liquid and supercritical CO₂. Ranges capture maximum and minimum values for all measurements performed for each test.

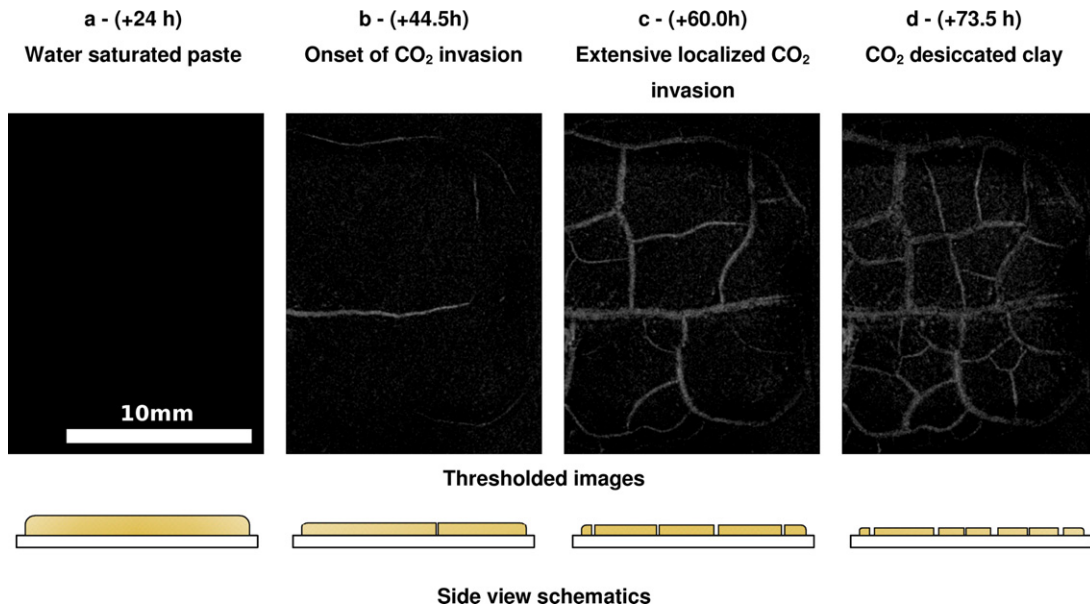


Fig. 6. Montmorillonite–water paste subjected to a supercritical CO_2 atmosphere (15 MPa, 311 K). Time lapse photography and associated sketches show the evolution of desiccation and the formation of capillary-driven fractures. The water– CO_2 interface initially “compresses” the sediment until supercritical CO_2 invades the sediment locally and triggers desiccation cracks.

“Water drying” results from the solubility of water in supercritical CO_2 , which reaches $\sim 5 \times 10^{-3}$ mol of water per mol of CO_2 at 15 MPa and 313 K, i.e., ~ 1.5 g of water per liter of CO_2 (water solubility in CO_2 data from [Spycher et al., 2003 – Table 3](#)). Water dissolves into the bulk CO_2 inside the chamber up to the limit of saturation (~ 0.3 g of water/210 cm^3 of CO_2 at 15 MPa and 313 K). We emphasize that there is no water inside the vessel besides the one in the bulk clay sediment.

The test procedure follows: (1) place 1.5 cm^3 of montmorillonite paste on a glass slide inside the chamber (clay mixed with 0.1 M NaCl solution at an initial water content of 1000%, i.e., $m_{\text{water}} = 10 \times m_{\text{clay}}$), (2) remove air and inject anhydrous CO_2 (research grade – Airgas), (3) pressurize to the target pressure–temperature supercritical conditions, and (4) monitor changes in the clay paste at steady temperature and pressure. While under pressure, we replaced the wet CO_2 with anhydrous CO_2 to promote further water drawing from the clay to the CO_2 . The CO_2 replacement process was implemented in a two-step sequence: (1) partial depressurization and leak-off to $P = 6$ MPa and (2) fast re-pressurization to the initial supercritical conditions.

4.2. Results

The clay paste contracted and cracked in the three experiments (two CO_2 replacement cycles). Snapshots in [Fig. 6](#) show images gathered at various stages in one test. During the first 48 h, water escapes the paste and dissolves into CO_2 ; there is significant volume contraction without cracking (not shown in the figure). Later on, as more water dissolves into the supercritical CO_2 , desiccation cracks gradually form ([Fig. 6](#)).

For the specific case shown in [Fig. 6](#), the initial height of the clay paste patch is ~ 4 mm, with an initial void ratio $e_0 = \omega G_s / S = 27$. After desiccation, the thickness of the thin clay crust is ~ 0.4 mm, the horizontal contraction is $\sim 20\%$, the volume has decreased by almost 12 times, the final void ratio of the clay crust pieces is about $e_f = (1 + e_0)V_0/V_f - 1 = 1.2$ (porosity $n \sim 0.55$; the analysis assumes that non-cracked crust pieces remain water-saturated), and the mean interparticle distance is $s = et \sim 1.2$ nm. Desiccation cracks

initiated extracting bulk water where the initial water content is very high in this demonstration test.

4.3. Analysis

The initiation mechanism for desiccation cracks can be explained within an effective stress framework in which capillary and skeletal forces compete ([Shin, 2009; Shin and Santamarina, 2010, 2011](#)). Discrete element numerical simulations corroborate the role of capillary forces in the development of fractures in fine-grained sediments ([Jain and Juanes, 2009](#)). The initial sediment compaction results from water loss which causes suction and the water– CO_2 interface to squeeze the clay paste. The void ratio decreases as suction $P_{\text{CO}_2} - P_w$ increases and follows 1D consolidation:

$$e = e_{1\text{kPa}} - C_c \log \left(\frac{P_{\text{CO}_2} - P_w}{1 \text{ kPa}} \right) \quad (11)$$

The consolidation parameters for this montmorillonite clay are $C_c = 0.46$ and $e_{1\text{kPa}} = 3$ (blue line in [Fig. 6b](#)). Eventually, as the differential pressure between water and CO_2 increases, the increasing clay stiffness prevents further consolidation; instead, the water– CO_2 interface invades the water saturated clay. The capillary entry value for parallel clay platelets, is computed using Laplace’s equation and the separation between platelets $t = 2e/(S_s \rho)$ as a function of the clay specific surface S_s and its mineral mass density ρ_m ,

$$P_{\text{CO}_2} - P_w \Big|_{\text{max}} = \frac{\rho_m T_s \cos \theta S_s}{10^\alpha e} \quad (12)$$

where the coefficient 10^α accounts for the pore size distribution within the clay mass $\alpha = \log(d^*)/\log(d_{\text{mean}})$, and d^* is the pore size at which capillary entry begins (note: the higher the α factor the wider the pore size distribution and the lower the value of capillary entry pressure – log-normal pore size distribution data and trends are explored in [Phadnis and Santamarina, 2011](#)). Clay particles remain water-wet in the presence of CO_2 (hydrophilic with $\theta \sim 40\text{--}60^\circ$ on silica surfaces – [Section 2.2](#)). As the mean direction of capillary forces is normal to the invading water– CO_2 interface, CO_2 invasion alters the distribution of particle forces from

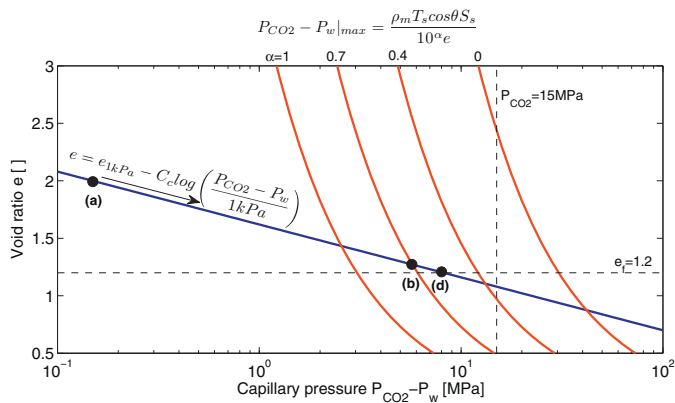


Fig. 7. Effective stress analysis of desiccation crack initiation. The clay paste starts at a high void ratio (point-a which corresponds to Fig. 6a) and follows the clay normal consolidation line (blue line) as it is compressed by the CO₂–water interface. The water–CO₂ interface invades the sediment when it reaches conditions that satisfy the capillary entry curve (red lines) for different α values where 10^α takes into account a log normal pore size distribution). Eventually, higher water suction forces the water–CO₂ interface to invade the sediment pore space (say point-b for $\alpha=0.7$). Interface invasion occurs at larger pores first, hence, these are nucleation sites for fracture initiation. The process ends when the mutual CO₂–water solubility is reached (point d which corresponds to Fig. 6d). Capillary-driven fractures will not form if the original effective stress is higher than the effective stress where the capillary entry curve and the normal consolidation line meet. (For interpretation of the references to color in this figure legend, the reader is referred to the web version of the article.)

vertical-dominant during consolidation, to transverse-dominant at invasion points leading to crack formation (Shin and Santamarina, 2011).

Fig. 7 shows in red a set of capillary entry value curves for different values of $\alpha > 0$. We can conclude that: (1) capillary entry and crack initiation cannot be explained considering a uniform pore size distribution $\alpha=0$ in these experiments as $P_{CO_2}-P_w$ would exceed 40 MPa; (2) CO₂ capillary entry starts at the largest voids, such as surface imperfections; (3) non-cracked clay crust pieces may remain water saturated; (4) CO₂ capillary drying reduces the clay porosity to levels equivalent to thousands of meters of overburden, and (5) while capillary forces may not cause desiccation cracks in highly overconsolidated low-porosity shales, they will produce tensile strains that may contribute to crack formation.

5. Discussion and implications

Buoyant scCO₂ in water creates a static overpressure which can reach $(\rho_w - \rho_{CO_2})hg \sim 0.4$ MPa for a $h=100$ m thick CO₂ pool ($\rho_{CO_2} \sim 720$ kg/m³ at $P=16$ MPa and $T=324$ K; $\rho_{CO_2} \sim 590$ kg/m³ at $P=16$ MPa and $T=339$ K). The CO₂ column height depends on the reservoir thickness, geometry, and injectability (capillary and viscous effects). Any excess injection pressure gradually dissipates due to CO₂ dissolution in water, residual water dissolution in CO₂, reservoir advective hydrogeology, and gravity-driven convection currents. The pressure discontinuity at the seal layer must be resisted by the seal's capillary entry resistance.

The assumption of a continuous seal leads to “upper bound seal capacity” estimates. Fractures, faults, and existing wellbores are major discontinuities that facilitate CO₂ leakage and lower the seal capacity. In addition, the caprock sealing capacity might be compromised by: (1) hydraulic fracture, (2) fault reactivation by reservoir overpressure (Chiaramonte et al., 2008; Rutqvist and Tsang, 2002), (3) CO₂ diffusion into the water saturated caprock (without bulk CO₂ invasion) and consequent water acidification and mineral dissolution (Berne et al., 2010; Gaus et al., 2005; Gherardi et al., 2007; Kohler et al., 2009; Shin et al., 2008); and (4) capillary breakthrough,

followed by CO₂ advection through the caprock (Angeli et al., 2009; Hildenbrand et al., 2004; Li et al., 2005; Wollenweber et al., 2010).

Additional electrical and capillary effects arise after CO₂ invasion of the caprock. Published studies reviewed above and new results presented in this manuscript are combined to anticipate the following potential sequence of events during the invasion of CO₂ into caprocks:

- The water–CO₂ interface reaches the caprock. The CO₂ pool creates a pressure discontinuity at the interface that is resisted by the caprock capillary entry value. CO₂ diffuses into the caprock while water dissolves into the CO₂.
- The pressure difference $P_{CO_2}-P_w$ exceeds the capillary entry pressure for CO₂ p_{CO_2} (entry) at surface imperfections and invades the largest pores first. Those become potential nuclei for fracture initiation.
- A percolating CO₂ path forms and CO₂ breaks through the caprock. The percolating path connects pores larger than the mean pore size in the caprock.
- Free ions migrate to the displaced water, yet counter ions remain to satisfy electroneutrality (see molecular simulations in Cole et al., 2010).
- Brine remains in smaller pores in the form of residual saturation. Part of the residual interparticle water dissolves in CO₂, the ionic concentration increases, electrical repulsion decreases, and excess salts precipitate. Residual water, CO₂, and precipitated salts eventually fill the interparticle space and dominate the interaction between clay platelets. The Hamaker constant increases ~ 3 times in clay–CO₂–clay compared to clay–water–clay systems, and particle attraction increases.
- Residual water acidifies due to CO₂ dissolution in water, and changes in pH modify the surface charge of clay particles. Changes in pH, ionic concentration, and Hamaker constant combine to cause fabric changes that can be analyzed in a pH-c₀ fabric map (Santamarina et al., 2001b).
- Continuous advective CO₂ flow will sustain water dissolution into scCO₂ (caprock dehydration), and cause further increase in suction leading to additional sediment contraction. The extent of dehydration will depend on the water content of the CO₂ and clay interlayer cation type. Anhydrous CO₂ can extract water from Na- and Ca-montmorillonite up to the 1W state, i.e., montmorillonite retains 1 monolayer of water; conversely, re-hydration may also occur if CO₂ contains enough dissolved water (Ilton et al., 2012; Schaefer et al., 2012).

While electrical and capillary effects are magnified in high specific surface clays, such as montmorillonite, the same effects will take place in other clays but will be moderated by particle size, and possible differences in surface charge (silica and gibbsite faces).

Desiccation tests show the effects of mutual water–CO₂ solubility, interfacial tension, suction, capillary-driven contraction, and the possible development of open-mode fractures. Capillary driven fractures are unlikely in low porosity caprocks at high effective stress (to the right of the capillary entry curve in Fig. 7). Given typical values of clay consolidation parameters (e_{1kPa} , C_c) and specific surface S_s (Burland, 1990; Santamarina et al., 2001a) and disregarding diagenetic cementation, we anticipate that capillary-driven fractures will not happen in kaolinite-, chlorite- or illite-rich shales at a burial depth greater than ~ 1 km. However, normally consolidated smectite-rich shales will remain prone to capillary effects to burial depths as high as ~ 4 km. The sequence of possible capillary-related events is captured in Fig. 8.

Related effects relevant to reservoir rocks. A relatively small fraction of clay minerals can easily affect the performance of reservoir rocks in CO₂ storage projects. For reference, let's define the

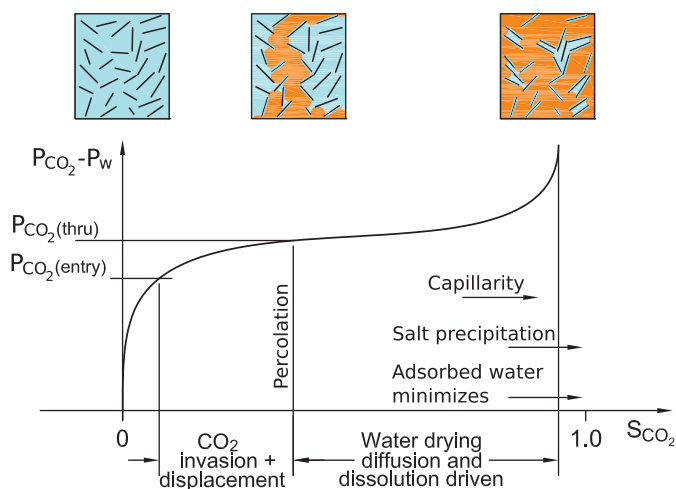


Fig. 8. CO₂ invasion into water saturated caprocks: capillary pressure and relative CO₂ saturation. As suction increases: (1) the sediment compresses, (2) capillary pressure overcomes the entry pressure; (3) desiccation fracture nuclei may develop, (4) a percolating path forms and CO₂ breaks through the medium, (5) water dissolves into scCO₂ until it reaches the equilibrium condition, suction increases, and excess salts precipitate.

critical clay mass fraction where clay particles fill the voids in the coarse-grained sediment skeleton

$$\frac{m_{\text{clay}}}{m_{\text{total}}} = \frac{e_{\text{coarse}}}{1 + e_{\text{coarse}} + e_{\text{clay}}} \quad (13)$$

where e_{coarse} and e_{clay} are the void ratios for the coarse grain structure and for the fines that fill the voids. Critical clay mass fractions can be less than $m_{\text{clay}}/m_{\text{total}} = 10\%$ for montmorillonite and 20% for kaolinite. Fines migration and clogging can severely restrict fluid flow even when the fines content is lower than these critical values.

Changes in electrical and capillary forces will affect fines in the reservoir as well. The injection of CO₂ into reservoirs may favor clay detachment from mineral surfaces (acidification and change in surface charge) or attachment (increased Hamaker constant). CO₂ may also open clay-filled pores by capillary driven contraction. Overall, we expect an increase in permeability in clayey sandstones during CO₂ invasion; indeed, experimental evidence shows that the water-measured intrinsic permeability of clay rich sandstones increases almost six fold after being flushed with CO₂ (Rimmele et al., 2010).

Finally, the permeability of clay-filled fractures and faults will also be adversely affected by clay sensitivity to CO₂. This situation must be carefully analyzed to estimate leakage potential.

6. Conclusions

Shales may serve as seal layers to retain pressurized and buoyant CO₂. Clay minerals determine the response of shale seals. Fine-grained clay fabrics have small pore size and can resist the pressure difference between the saturating water and the buoyant CO₂ pool. However, clayey sediments are susceptible to electrical and capillary forces.

The electrical interaction between clay particles is different in CO₂ than in water. The analysis of inter-particle forces shows a decrease in electrical repulsion and an increase in electrical attraction in CO₂ compared to water. In particular, Lifschitz theory predicts a three-fold increase in the Hamaker constant from clay–water–clay to clay–CO₂–clay systems.

Interfacial tension brings about capillary forces in water–CO₂–mineral systems. Gradually, water dissolves into the CO₂ and suction increases in the seal layer.

The change in electrical forces and the emergence of capillary effects anticipates volume contraction following the injection of CO₂ in initially water-saturated formations.

Open-mode fractures could develop in normally consolidated clayey seals. Initiation conditions depend on burial depth, mineralogy and pore size distribution. Localized CO₂ flow would ensue and hinder the sealing capacity of caprocks.

The advection of CO₂ after breakthrough promotes further water dissolution in CO₂, the dehydration of the seal layer, and increased suction.

Similar chemo-hydro-mechanical couplings affect clay particles in reservoir rocks, fractures, and fault fillings.

Phenomena discussed in this manuscript have been individually confirmed/observed in this research and/or reported in published studies. Yet, the complex interplay between chemo-hydro-mechanical processes may lead to positive feedback mechanisms that can either degrade (e.g., clay platelet collapse → sediment contraction and fracturing → further fluid conduction) or self-stabilize (e.g., water dissolution in CO₂ → salt precipitation from brine → porosity reduction) the caprock seal capacity, or alter CO₂ injectability into the reservoir.

Experiments reported in this study were designed to enhance the phenomena under consideration, and emphasized conditions at large interparticle distances. Additional research is needed to further assess coupled phenomena when the interparticle distance is equivalent to a few monolayers of water, as in mormorillonitic shales.

Acknowledgments

This material is based upon work supported by the U.S. Department of Energy (DOE) National Energy Technology Laboratory (NETL) under Grant Number DEFE0001826. Additional support was provided by the The Goizueta Foundation. Any opinions, findings, conclusions, or recommendations expressed herein are those of the authors and do not necessarily reflect the views of funding organizations. K. Olson helped in the execution of sedimentation tests; C. Barrett edited the manuscript. We are grateful to anonymous reviewers for insightful comments and suggestions.

References

- Alonso, E.E., Gens, A., Josa, A., 1990. A constitutive model for partially saturated soils. *Geotechnique* 40, 405–430.
- Angeli, M., Soldal, M., Skurtveit, E., Aker, E., 2009. Experimental percolation of supercritical CO₂ through a caprock. In: Gale, J., Herzog, H., Braitsch, J. (Eds.), *Greenhouse Gas Control Technologies*, vol. 9, pp. 3351–3358.
- Armitage, P.J., Worden, R.H., Faulkner, D.R., Aplin, A.C., Butcher, A.R., Iliffe, J., 2010. Diagenetic and sedimentary controls on porosity in lower carboniferous fine-grained lithologies, Krechba field, Algeria: a petrological study of a caprock to a carbon capture site. *Marine and Petroleum Geology* 27, 1395–1410.
- Aucejo, A., Burguet, M.C., Munoz, R., Marques, J.L., 1995. Densities, viscosities, and refractive-indexes of some n-alkane binary-liquid systems at 298.15-K. *Journal of Chemical and Engineering Data* 40, 141–147.
- Benison, K.C., Goldstein, R.H., 2000. Sedimentology of ancient saline pans: an example from the Permian Opeche Shale, Williston Basin, North Dakota, USA. *Journal of Sedimentary Research* 70, 159–169.
- Berne, P., Bachaud, P., Fleury, M., 2010. Diffusion properties of carbonated caprocks from the Paris Basin. *Oil & Gas Science and Technology – Revue De L Institut Francais Du Petrole* 65, 473–484.
- Bøe, R., Zweigel, P., 2001. Characterisation of the Nordland Shale in the Sleipner area by XRD analysis – A contribution to the Saline Aquifer CO₂ Storage (SACS) project. SINTEF Technical Reports.
- Borysenko, A., Clennell, B., Sedev, R., Bugar, I., Ralston, J., Raven, M., Dewhurst, D., Liu, K., 2009. Experimental investigations of the wettability of clays and shales. *Journal of Geophysical Research* 114. <http://dx.doi.org/10.1029/2008JB005928>.
- Botan, A., Rotenberg, B., Marry, V., Turq, P., Noetinger, B., 2010. Carbon dioxide in montmorillonite clay hydrates: thermodynamics, structure, and transport from molecular simulation. *Journal of Physical Chemistry C* 114, 14962–14969.
- Buchner, R., Hefter, G.T., May, P.M., 1999. Dielectric relaxation of aqueous NaCl solutions. *Journal of Physical Chemistry A* 103, 1–9.
- Burland, J.B., 1990. On the compressibility and shear strength of natural clays. *Geotechnique* 40, 329–378.

- Busch, A., Alles, S., Gensterblum, Y., Prinz, D., Dewhurst, D.N., Raven, M.D., Stanjek, H., Krooss, B.M., 2008. Carbon dioxide storage potential of shales. *International Journal of Greenhouse Gas Control* 2, 297–308.
- Carey, J.W., Wigand, M., Chipera, S.J., WoldeGabriel, G., Pawar, R., Lichtner, P.C., Wehner, S.C., Raines, M.A., Guthrie, J.G.D., 2007. Analysis and performance of oil well cement with 30 years of CO₂ exposure from the SACROC Unit, West Texas, USA. *International Journal of Greenhouse Gas Control* 1, 75–85.
- Chadwick, R.A., Zweigel, P., Gregersen, U., Kirby, G.A., Holloway, S., Johannessen, P.N., 2004. Geological reservoir characterization of a CO₂ storage site: The Utsira Sand, Sleipner, Northern North Sea. *Energy* 29, 1371–1381.
- Chalabaud, C., Robin, M., Lombard, J.M., Martin, F., Egermann, P., Bertin, H., 2009. Interfacial tension measurements and wettability evaluation for geological CO₂ storage. *Advances in Water Resources* 32, 98–109.
- Chi, S.M., Morsi, B.I., Klinzing, G.E., Chiang, S.H., 1988. Study of interfacial properties in the liquid CO₂ water coal system. *Energy & Fuels* 2, 141–145.
- Chiaromonte, L., Zoback, M., Friedmann, J., Stamp, V., 2008. Seal integrity and feasibility of CO₂ sequestration in the Teapot Dome EOR pilot: geomechanical site characterization. *Environmental Geology* 54, 1667–1675.
- Chiquet, P., Broseta, D., Thibeau, S., 2007. Wettability alteration of caprock minerals by carbon dioxide. *Geofluids* 7, 112–122.
- Cole, D.R., Chialvo, A.A., Rother, G., Vlcek, L., Cummings, P.T., 2010. Supercritical fluid behavior at nanoscale interfaces: implications for CO₂ sequestration in geologic formations. *Philosophical Magazine* 90, 2339–2363.
- Dewhurst, D.N., Jones, R.M., Raven, M.D., 2002. Microstructural and petrophysical characterization of Muderong Shale: application to top seal risking. *Petroleum Geoscience* 8, 371–383, doi:10.1144/petgeo.1144.1144.1371.
- Dickson, J.L., Gupta, G., Horozov, T.S., Binks, B.P., Johnston, K.P., 2006. Wetting phenomena at the CO₂/water/glass interface. *Langmuir* 22, 2161–2170.
- Dooley, J.J., Dahowski, R., Davidson, C., Wise, M.A., Gupta, N., Kim, S.H., Malone, E.L., 2006. Carbon Dioxide Capture and Geologic Storage: A Core Element of a Global Energy Technology Strategy to Address Climate Change. PNNL, Richland, WA.
- Downey, M.W., 1984. Evaluating seals for hydrocarbon accumulations. *AAPG Bulletin* 68, 1752–1763.
- Espinoza, D.N., Santamarina, J.C., 2010. Water–CO₂–mineral systems: interfacial tension, contact angle and diffusion – Implications to CO₂ geological storage. *Water Resources Research* 46, <http://dx.doi.org/10.1029/2009WR008634>.
- Fahmy, T.M., Paulaitis, M.E., Johnson, D.M., McNally, M.E.P., 1993. Modifier effects in the supercritical fluid extraction of solutes from clay, soil, and plant materials. *Analytical Chemistry* 65, 1462–1469.
- Fenghour, A., Wakeham, W.A., Vesovic, V., 1998. The viscosity of carbon dioxide. *Journal of Physical and Chemical Reference Data* 27, 31–44.
- Ferrage, E., Lanson, B., Sakharov, B.A., Drits, V.A., 2005. Investigation of smectite hydration properties by modeling experimental X-ray diffraction patterns. Part I. Montmorillonite hydration properties. *American Mineralogist* 90, 1358–1374.
- Förster, A., Springer, N., Beutler, G., Luckert, J., Norden, B., Lindgren, H., 2007. The mudstone-dominated caprock system of the CO₂-storage site at Ketzin, Germany. In: AAPG Annual Convention, Long Beach, CA.
- Friiso, T., Tjomsland, T., 1997. Monitoring of density changes in low-permittivity liquids by microwave-permittivity measurements with an open-ended probe. *Measurement Science & Technology* 8, 1295–1305.
- Gale, J., 2004. Geological storage of CO₂: what do we know, where are the gaps and what more needs to be done? *Energy* 29, 1329–1338.
- Gaus, I., Azaroual, M., Czernichowski-Lauriol, I., 2005. Reactive transport modelling of the impact of CO₂ injection on the clayey cap rock at Sleipner (North Sea). *Chemical Geology* 217, 319–337.
- Gherardi, F., Xu, T.F., Pruess, K., 2007. Numerical modeling of self-limiting and self-enhancing caprock alteration induced by CO₂ storage in a depleted gas reservoir. *Chemical Geology* 244, 103–129.
- Giesting, P., Guggenheim, S., Koster van Groos, A.F., Busch, A., 2012. Interaction of carbon dioxide with Na-exchanged montmorillonite at pressures to 640 bars: implications for CO₂ sequestration. *International Journal of Greenhouse Gas Control* 8, 73–81.
- Gueguen, Y., Palciauskas, V., 1994. *Introduction to the Physics of Rocks*. Princeton University Press.
- Han, W.S., McPherson, B.J., Lichtner, P.C., Wang, F.P., 2010. Evaluation of trapping mechanisms in geologic CO₂ sequestration: case study of SACROC northern platform, a 35-year CO₂ injection site. *American Journal of Science* 310, 282–324.
- Hildenbrand, A., Schlomer, S., Krooss, B.M., Littke, R., 2004. Gas breakthrough experiments on pelitic rocks: comparative study with N₂, CO₂ and CH₄. *Geofluids* 4, 61–80.
- Hovorka, S.D., 2009. Frio brine pilot: the first U.S. sequestration test. *Southwest Hydrology* September/October.
- Hundal, L.S., Thompson, M.L., Laird, D.A., Carmo, A.M., 2001. Sorption of phenanthrene by reference smectites. *Environmental Science & Technology* 35, 3456–3461.
- Ilton, E.S., Schaeff, H.T., Qafoku, O., Rosso, K.M., Felmy, A.R., 2012. In situ X-ray diffraction study of Na⁺ saturated montmorillonite exposed to variably wet supercritical CO₂. *Environmental Science & Technology* 46, 4241–4248.
- IPCC Special Report on Carbon Dioxide Capture and Storage, 2005. In: Metz, B., Davidson, O., de Coninck, H.C., Loos, M., Meyer, L.A. (Eds.), Prepared by Working Group III of the Intergovernmental Panel on Climate Change. Cambridge University Press, Cambridge, United Kingdom and New York, NY, USA.
- Israelachvili, J., 1991. *Intermolecular and Surface Forces*, 2nd ed. Academic Press, London.
- Jain, A.K., Juanes, R., 2009. Preferential mode of gas invasion in sediments: grain-scale mechanistic model of coupled multiphase fluid flow and sediment mechanics. *Journal of Geophysical Research* 114, <http://dx.doi.org/10.1029/2008JB006002>.
- Jo, H.Y., Katsumi, T., Benson, C.H., Edil, T.B., 2001. Hydraulic conductivity and swelling of nonhydrated GCLs permeated with single-species salt solutions. *Journal of Geotechnical and Geoenvironmental Engineering* 127, 557–567.
- Katsube, T.J., Williamson, M.A., 1994. Effects of diagenesis on shale nano-pore structure and implications for sealing capacity. *Clay Minerals* 29, 451–461.
- Kaya, A., Fang, H.Y., 2005. Experimental evidence of reduction in attractive and repulsive forces between clay particles permeated with organic liquids. *Canadian Geotechnical Journal* 42, 632–640.
- Kohler, E., Parra, T., Vidal, O., 2009. Clayey cap-rock behavior in H₂O–CO₂ media at low pressure and temperature conditions: an experimental approach. *Clays and Clay Minerals* 57, 616–637.
- Kvamme, B., Kuznetsova, T., Hebach, A., Oberhof, A., Lunde, E., 2007. Measurements and modelling of interfacial tension for water plus carbon dioxide systems at elevated pressures. *Computational Materials Science* 38, 506–513.
- Leach, E.S.H., Hopkinson, A., Franklin, K., van Duijneveldt, J.S., 2005. Non-aqueous suspensions of laponite and montmorillonite. *Langmuir* 21, 3821–3830.
- Lewis, J.E., Biswas, R., Robinson, A.G., Maroncelli, M., 2001. Local density augmentation in supercritical solvents: electronic shifts of anthracene derivatives. *Journal of Physical Chemistry B* 105, 3306–3318.
- Li, S., Dong, M., Li, Z., Huang, S., Qing, H., Nickel, E., 2005. Gas breakthrough pressure for hydrocarbon reservoir seal rocks: implications for the security of long-term CO₂ storage in the Weyburn field. *Geofluids* 5, 326–334.
- Lyklema, J., 1995. *Fundamentals of Interface and Colloid Science. Volume II: Solid–Liquid Interfaces*. Academic Press, New York.
- Lynch, F.L., 1997. Frio shale mineralogy and the stoichiometry of the smectite-to-illite reaction: the most important reaction in clastic sedimentary diagenesis. *Clays and Clay Minerals* 45, 618–631.
- Mathieson, A., Midgley, J., Dodds, J., Wright, I., Ringrose, P., Saoul, N., 2010. CO₂ sequestration monitoring and verification technologies applied at Krecbba, Algeria. *The Leading Edge* 29, 216–222.
- May, E.F., Moldover, M.R., Schmidt, J.W., 2005. The dielectric permittivity of saturated liquid carbon dioxide and propane measured using cross capacitors. *International Journal of Thermophysics* 26, 563–576.
- Maykut, G.A., Light, B., 1995. Refractive-index measurements in freezing sea-ice and sodium-chloride brines. *Applied Optics* 34, 950–961.
- Mitchell, J.K., Soga, K., 2005. *Fundamentals of Soil Behavior*, 3rd ed. Wiley.
- Montoro, M., Francisca, F., 2010. Soil permeability controlled by particle–fluid interaction. *Geotechnical and Geological Engineering* 28, 851–864.
- Nygaard, R., Gutierrez, M., Hoeg, K., Bjorlykke, K., 2004. Influence of burial history on microstructure and compaction behaviour of Kimmeridge clay. *Petroleum Geoscience* 10, 259–270.
- Obriot, J., Ge, J., Bose, T.K., Starnaud, J.M., 1993. Determination of the density from simultaneous measurements of the refractive-index and the dielectric-constant of gaseous CH₄, SF₆ and CO₂. *Fluid Phase Equilibria* 86, 315–350.
- Palomino, A.M., 2003. *Fabric Formation and Control in Fine-grained Materials*. Georgia Institute of Technology, Atlanta.
- Palomino, A.M., Santamarina, J.C., 2005. Fabric map for kaolinite: effects of pH and ionic concentration on behavior. *Clays and Clay Minerals* 53, 211–223.
- Phadnis, H.S., Santamarina, J.C., 2011. Bacteria in sediments: pore size effects. *Geotechnique Letters* 1, 91–93.
- Pillitteri, A., Cerasi, P., Stavrum, J., Zweigel, P., Bøe, R., 2003. Rock mechanical tests of shale samples from the cap rock of the Utsira Sand in well 15/9-A11. SINTEF Petroleum Research.
- Polak, J., Lu, B.C.Y., 1973. Mutual solubilities of hydrocarbons and water at 0 and 25 °C. *Canadian Journal of Chemistry – Revue Canadienne De Chimie* 51, 4018–4023.
- Rimmele, G., Barlet-Gouedard, V., Renard, F., 2010. Evolution of the petrophysical and mineralogical properties of two reservoir rocks under thermodynamic conditions relevant for CO₂ geological storage at 3 km depth. *Oil & Gas Science and Technology – Revue De L Institut Francais Du Pétrole* 65, 565–580.
- Robinson, D.A., 2004. Measurement of the solid dielectric permittivity of clay minerals and granular samples using a time domain reflectometry immersion method. *Vadose Zone Journal* 3, 705–713.
- Rutqvist, J., Tsang, C., 2002. A study of caprock hydromechanical changes associated with CO₂-injection into a brine formation. *Environmental Geology* 42, 296–305.
- Santamarina, J.C., 2001. Soil behavior at the microscale: particle forces. In: *Symp. Soil Behavior and Soft Ground Construction*, in honor of Charles C. Ladd, MIT.
- Santamarina, J.C., Klein, K.A., Fam, M.A., 2001a. *Soils and Waves*. Wiley.
- Santamarina, J.C., Klein, K.A., Palomino, A., Guimaraes, M.S., 2001b. Micro-scale aspects of chemical-mechanical coupling: interparticle forces and fabric. In: Maio, C.D., Hueckel, T., Loret, B. (Eds.), *Chemo-mechanical Coupling in Clays – from Nano-scale to Engineering Applications*.
- Santamarina, J.C., Klein, K.A., Wang, Y.H., Prencke, E., 2002. Specific surface: determination and relevance. *Canadian Geotechnical Journal* 39, 233–241.
- Schaeff, H.T., Ilton, E.S., Qafoku, O., Martin, P.F., Felmy, A.R., Rosso, K.M., 2012. In situ XRD study of Ca²⁺ saturated montmorillonite (STX-1) exposed to anhydrous and wet supercritical carbon dioxide. *International Journal of Greenhouse Gas Control* 6, 220–229.
- Serhatkulu, G.K., Dilek, C., Gulari, E., 2006. Supercritical CO₂ intercalation of layered silicates. *Journal of Supercritical Fluids* 39, 264–270.
- Shin, H., 2009. *Development of Discontinuities in Granular Media*. Georgia Institute of Technology.

- Shin, H., Santamarina, J.C., 2010. Fluid-driven fractures in uncemented sediments: underlying particle-level processes. *Earth and Planetary Science Letters* 299, 180–189.
- Shin, H., Santamarina, J.C., 2011. Desiccation cracks in saturated fine-grained soils: particle level phenomena and effective stress analysis. *Geotechnique* 61, 961–972.
- Shin, H., Santamarina, J.C., Cartwright, J.A., 2008. Contraction-driven shear failure in compacting uncemented sediments. *Geology* 36, 931–934.
- Span, R., Wagner, W., 1996. A new equation of state for carbon dioxide covering the fluid region from the triple-point temperature to 1100 K at pressures up to 800 MPa. *Journal of Physical and Chemical Reference Data* 25, 1509–1596.
- Sposito, G., 1989. *The Chemistry of Soils*. Oxford University Press, New York.
- Spycher, N., Pruess, K., Ennis-King, J., 2003. CO₂–H₂O mixtures in the geological sequestration of CO₂. I. Assessment and calculation of mutual solubilities from 12 to 100 °C and up to 600 bar. *Geochimica Et Cosmochimica Acta* 67, 3015–3031.
- Stumm, W., 1992. *Chemistry of the Solid–Water Interface*. Wiley, New York.
- Sun, Y.D., Shekunov, B.Y., York, P., 2003. Refractive index of supercritical CO₂–ethanol solvents. *Chemical Engineering Communications* 190, 1–14.
- Susilo, R., Lee, J.D., Englezos, P., 2005. Liquid–liquid equilibrium data of water with neohexane, methylcyclohexane, tert-butyl methyl ether, *n*-heptane and vapor–liquid–liquid equilibrium with methane. *Fluid Phase Equilibria* 231, 20–26.
- Tonnet, N., Mouronval, G., Chiquet, P., Broseta, D., 2011. Petrophysical assessment of a carbonate-rich caprock for CO₂ geological storage purposes. *Energy Procedia* 4, 5422–5429.
- Urbanczyk, L., Calberg, C., Detrembleur, C., Jerome, C., Alexandre, M., 2010. Batch foaming of SAN/clay nanocomposites with scCO₂: a very tunable way of controlling the cellular morphology. *Polymer* 51, 3520–3531.
- Van Olphen, H., 1977. *An Introduction to Clay Colloid Chemistry: For Clay Technologists, Geologists, and Soil Scientists*, 2nd ed. Wiley, New York.
- van Oort, E., 2003. On the physical and chemical stability of shales. *Journal of Petroleum Science and Engineering* 38, 213–235.
- Vandeweyer, V., van der Meer, B., Hofstee, C., Mulders, F., D'Hoore, D., Graven, H., 2011. Monitoring the CO₂ injection site: K12-B. *Energy Procedia* 4, 5471–5478.
- Watson, M.N., Daniel, R.F., Tingate, P.R., Gibson-Poole, C.M., 2005. CO₂ related seal capacity enhancement in mudstones: evidence from the pine lodge natural CO₂ accumulation, Otway Basin, Australia. In: Rubin, E.S., Keith, D.W., Gilboy, C.F. (Eds.), *International Conference on Greenhouse Gas Control Technologies*. Vancouver, Canada, 2004.
- Weidler, P.G., Friedrich, F., 2007. Determination of the refractive index of particles in the clay and sub-micrometer size range. *American Mineralogist* 92, 1130–1132.
- Wollenweber, J., Alles, S., Busch, A., Krooss, B.M., Stanjek, H., Littke, R., 2010. Experimental investigation of the CO₂ sealing efficiency of caprocks. *International Journal of Greenhouse Gas Control* 4, 231–241.
- Zeppieri, S., Rodriguez, J., de Ramos, A.L.L., 2001. Interfacial tension of alkane plus water systems. *Journal of Chemical and Engineering Data* 46, 1086–1088.
- Zhang, H.L., Han, S.J., 1996. Viscosity and density of water plus sodium chloride plus potassium chloride solutions at 298.15 K. *Journal of Chemical and Engineering Data* 41, 516–520.